ACS OMEGA

Open Access

http://pubs.acs.org/journal/acsodf

Article

Effect of Rh Loading on the Performance of Rh/CeO_2 in CH_4 Combustion: Important Role of Forming RhO_x Nanoparticles

Chenxin Xu,[○] Tian Qin,[○] Ze-Kai Yu,[○] Zhi-Qiang Wang,[○] Liwei Chen, Yaxin Chen,[*] Xingfu Tang,[*] Xi Liu,[*] Xue-Qing Gong,[*] and Zhen Ma[*]

Cite This: ACS Omega 2025, 10, 18682−18689

Read Online

ABSTRACT: In order to avoid the emission of CH_4 into the air, catalytic combustion of CH_4 is a practical solution, but it is challenging to develop efficient catalysts due to the inertness of CH_4. Herein, Rh/CeO_2 catalysts with different Rh loadings were synthesized and compared. The catalytic activities in CH_4 oxidation were found to increase with an increase of Rh loading. Thus, $0.3Rh/CeO_2$ (with 0.3 wt % Rh) and $2.0Rh/CeO_2$ (with 2.0 wt % Rh) were chosen as representatives to study the difference. It was found that the Rh species exist as Rh single atoms with a valence of +3 in $0.3Rh/CeO_2$, and there are RhO_x nanoparticles showing the coexistence of Rh^{3+} and $Rh^{\delta+}$ in $2.0Rh/CeO_2$. Theoretical calculations show that, in the CeO_2-supported RhO_x nanoparticles catalyst, the band gap between the highest occupied band orbital and the lowest unoccupied band orbital of CeO_2 is filled with the Rh density of state, while there remains a gap of ~0.6 eV for the single-atom catalyst. The smaller gap between the highest occupied band orbitals and the lowest unoccupied band orbitals makes the RhO_x nanoparticles more favorable for electron transfer than the single-atom catalyst, resulting in a lower energy barrier in C−H bond activation and higher catalytic activity. This work provides a rationale for developing high-activity catalysts for CH_4 oxidation.

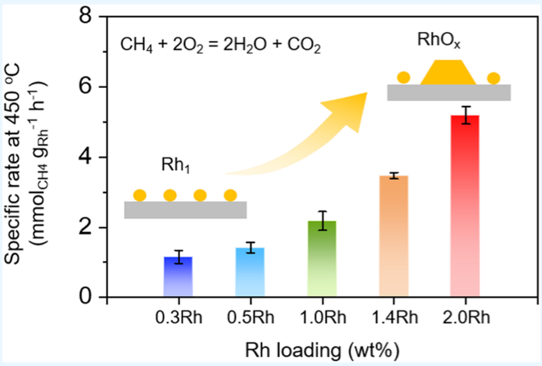

1. INTRODUCTION

Methane (CH_4), being a clean energy carrier, has been widely used in natural gas vehicles, natural gas dual-fuel tankers, and other energy fields. In practical applications, incomplete utilization of CH_4 will lead to the release of CH_4 (a greenhouse gas) into the air. Catalytic combustion is an effective method to avoid the emission of CH_4.[1−4] However, CH_4 is highly stable, and active oxygen species are needed for CH_4 combustion, so the catalyst needs to have excellent ability for activating CH_4 and O_2 at low temperatures.

The breaking of the C−H bond is generally considered as the rate-determining step of CH_4 oxidation.[5] Noble metal catalysts have been widely studied in CH_4 oxidation due to their special electronic state of the d-band and strong ability for activating the C−H bond.[6] In theoretical studies, Rh is the most active metal for activating the C−H bond.[7] In experimental studies, Rh-based catalysts also show strong CH_4 activation ability and high catalytic activity in the complete oxidation of CH_4.[8−14] Therefore, it is meaningful to study Rh-based catalysts in catalytic CH_4 oxidation.

The oxygen activation ability of a catalyst is closely related to the electron supply capacity of the catalyst to adsorb oxygen.[15] Among various supports, CeO_2 shows excellent redox performance. The rapid transformation between Ce^{4+} and Ce^{3+} renders the surface of CeO_2 with abundant oxygen vacancies,[16,17] which is conducive to the generation of active oxygen species. In addition, the strong metal-support interaction between CeO_2 and noble metals can stably bind the active phase of the noble metal.[18] Therefore, CeO_2 is an excellent oxide support in designing catalysts for CH_4 oxidation.

Herein, Rh/CeO_2 catalysts with different Rh loadings were prepared, and the activity trend in CH_4 oxidation as the Rh loading increases was observed. $0.3Rh/CeO_2$ (with 0.3 wt % Rh) and $2.0Rh/CeO_2$ (with 2.0 wt % Rh) were selected as representative catalysts, and their geometric and electronic structures were analyzed to explain the reasons for the differences in catalytic performance.

2. EXPERIMENTAL SECTION

2.1. Catalyst Preparation. CeO_2 nanorods were synthesized by a hydrothermal method using $Ce(NO_3)_3$ as the cerium source.[19] 1.562 g $Ce(NO_3)_3 \cdot 6H_2O$ was dissolved into 9 mL of ultrapure water. An aqueous NaOH solution (C_{NaOH} = 6 M, 63 mL) was transferred into a 100 mL Teflon bottle. The

Received: January 3, 2025
Revised: March 30, 2025
Accepted: April 15, 2025
Published: April 28, 2025

https://doi.org/10.1021/acsomega.5c00062
ACS Omega 2025, 10, 18682−18689

$Ce(NO_3)_3$ solution was added into the NaOH solution drop by drop to obtain a suspension, and then the suspension was stirred for 0.5 h. The Teflon bottle was placed into a stainless-steel autoclave, and the autoclave was transferred to an oven for heating at 100 °C for 24 h. The lavender precipitate was washed with ultrapure water until the pH of the supernatant was 7. The dark green product, obtained by further filtering, was transferred to an oven for drying at 80 °C overnight to obtain a light-yellow solid. After grinding, it was placed in a muffle furnace, heated to 300 °C at a ramping rate of 2 °C min^{-1}, and then calcined at 300 °C for 4 h to obtain CeO_2 nanorods.

Rh/CeO_2 catalysts with different Rh loadings were prepared by conventional wet impregnation. First, 1 g of CeO_2 was dispersed in 40 mL of ultrapure water, and an $(NH_4)_3RhCl_6$ solution (4.03 mg_{Rh} mL^{-1}) was added with a corresponding volume to reach the desired Rh loading. The suspension was stirred at 80 °C until it was dry. The obtained solid was dried at 80 °C overnight, calcined in a muffle furnace at 400 °C for 4 h, and cooled for collection. The ramping rate before reaching 400 °C was 2 °C min^{-1}. The Rh loadings of each catalyst are given in Table S1.

2.2. Catalyst Characterization. All the samples used in characterization (except for those used in ICP analysis) refer to the powder catalysts collected after $CH_4 + O_2$ treatment at 800 °C, i.e., the catalyst (80−100 mesh, without adding Si_3N_4 particles) was transferred to a catalytic reactor (which is also used in catalytic testing in this study), heated to 800 °C at a ramping rate of 2 °C min^{-1} in 100 mL min^{-1} mixed gas (composed of 50 ppm of CH_4, 20 vol % O_2, and balance Ar), maintained at 800 °C for 1 h, and cooled down for collection. The collected catalyst was grinded to fine powders in a agate mortar.

X-ray diffraction (XRD) patterns were recorded on an X-ray diffractometer (D8 Advance). The Rh loadings of the catalysts were measured by inductive coupled plasma optical emission spectroscopy (ICP-OES). Transmission electron microscopy (TEM) and high-resolution TEM (HRTEM) images were recorded by a transmission electron microscope (JEOL JEM-2100F). Scanning TEM (STEM) images were recorded with an aberration-corrected scanning/transmission electron microscope (Hitachi HF5000), operated at 200 kV. X-ray photoelectron spectra (XPS) were collected on a Kratos Axis Ultra DLD system using a monochromatic Al-Kα X-ray source ($h\upsilon$ = 1486.6 eV). Spectra were all referenced to the C 1s peak with a binding energy of 284.8 eV. Data analysis and processing were undertaken using XPS Peak4.1 using Shirley-type background. Diffuse reflectance infrared Fourier transform spectra (DRIFTS) were recorded on a Fourier-transform infrared (FTIR) spectrometer (Nicolet iS-50). The sample was first pretreated at 300 °C in pure N_2 (100 mL min^{-1}) for 1 h, and then cooled to 35 °C. Background data were collected after pretreatment at 35 °C, and then the gas flow was changed to 1% CO/He (50 mL min^{-1}) for 30 min until adsorption saturation. Finally, the sample was purged in a N_2 flow (100 mL min^{-1}) for 20 min to remove physically adsorbed CO on the sample's surface. The CO-DRIFT spectra were obtained by subtracting the background spectra. X-ray absorption (XAS) data were recorded at room temperature in a transmission mode using ion chambers at beamline BL14W1 of the Shanghai Synchrotron Radiation Facility (SSRF) in China. The data at the Rh *K*-edge were collected with a fixed exit monochromator using a Si(311) crystal. The raw data were analyzed using the IFEFFIT 1.2.11 software package.

2.3. Density Function Theory (DFT) Calculations. DFT calculations were performed using the Vienna Ab-initio Simulation Package (VASP) with the projector augmented wave (PAW) method[20] and the Perdew−Burke−Ernzerhof (PBE)[21] functional under the generalized gradient approximation (GGA).[22] The kinetic energy cutoff was set as 400 eV. Structure optimizations were finished until the force was lower than 0.05 eV $Å^{-1}$. The interaction between neighboring slabs was eliminated by a large vacuum gap of 12 Å. A $p(5 \times 5)$ surface slab containing three O−Ce−O layers was built as the model constructure for the $CeO_2(111)$ surface. The top two layers of the slabs were allowed to relax, and the bottom layer was kept fixed to mimic the bulk region. A *k*-point mesh of 2 × 2 × 1 was adopted for Brillouin-zone integrations.[23] The U value to describe the localized 4*f* orbitals of Ce was set as 5.0 eV.[24,25] Rh_6O_{12} nanoparticles on $CeO_2(111)$ and Rh single atoms coordinating with four oxygen atoms over $CeO_2(111)$ were constructed to simulate Rh_6O_{12}/CeO_2 and Rh_1/CeO_2.

2.4. Catalytic Evaluation. The conversion curves of the samples were tested in a quartz glass fixed-bed flow reactor. A 100 mg catalyst (80−100 mesh) was diluted with 300 mg of Si_3N_4 particles. The mixture was transferred to the catalytic reactor, heated to 800 °C at a ramping rate of 2 °C min^{-1} in 100 mL min^{-1} mixed gas (composed of 50 ppm of CH_4, 20 vol % O_2, and balance Ar), maintained at 800 °C for 1 h, and cooled down, without being taken out. The sample was then treated at 300 °C in a N_2 flow (100 mL min^{-1}) for 30 min and cooled down. Pure CeO_2 pretreated in N_2 at 300 °C (without being pretreated in CH_4 +O_2 at 800 °C) was tested for comparison.

The experimental feed gas was composed of 50 ppm of CH_4, 20 vol % O_2, and balance Ar, and the total flow rate was 100 mL min^{-1}. The catalyst was heated from 30 to 800 °C at a ramping rate of 2 °C min^{-1}. Data were collected by an online gas chromatograph (Agilent 7890A) equipped with a flame ionization detector (FID) and a thermal conductivity detector (TCD). A detailed schematic diagram of the testing device for catalyst evaluation is shown in Figure S1.

3. RESULTS AND DISCUSSION

Using CeO_2 nanorods as the support, Rh/CeO_2 catalysts with different Rh loadings were prepared and tested in CH_4 oxidation. As shown in Figure 1, the activities of Rh/CeO_2 catalysts gradually increase with the increase of Rh loading, and the data show good repeatability (Figure S2). The conversion

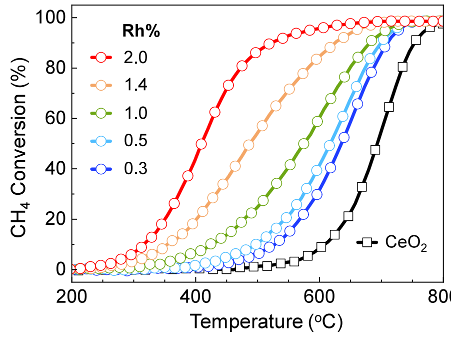

Figure 1. Conversion curves of CH_4 over Rh/CeO_2 (pretreated in $CH_4 + O_2$ at 800 °C) with different loadings.

https://doi.org/10.1021/acsomega.5c00062
ACS Omega 2025, 10, 18682−18689

of CH_4 on Rh/CeO_2 with Rh loadings of 0.3, 0.5, 1.0, 1.4, and 2.0 at 450 °C is 2.7, 4.8, 13.4, 35.7, and 71.4%, respectively, and the corresponding specific rates, calculated according to the actual Rh loadings determined by ICP (Table S1) are 1.2, 1.3, 1.9, 3.6, and 5.0 $mmol_{CH4}\ g_{Rh}^{-1}\ h^{-1}$, respectively (Table S2). CeO_2 can stabilize single Pt,[26] Pd,[27] and Rh[28] atoms, and the capacity for loading Rh single atoms on the current CeO_2 support is estimated to be 0.7 wt % (Note S1). Thus, $2.0Rh/CeO_2$ containing 2.0 wt % Rh is supposed to contain nanoparticles since the Rh loading far exceeds the threshold value.[29] Next, we selected $0.3Rh/CeO_2$ and $2.0Rh/CeO_2$ with Rh loadings below and above the threshold value for a detailed study.

The XRD pattern of CeO_2 shows the cubic structure of CeO_2 (Figure 2), and the peaks at 2θ = 28.5°, 33.1°, 47.5°, and 56.3° represent the (111), (200), (220), and (311) planes, respectively. Rh/CeO_2 catalysts maintain the cubic CeO_2 structure, and no Rh species can be observed, indicating that Rh species are highly dispersed. The introduction of Rh on CeO_2 can make the (111) peak shift to a higher 2θ angle. This change is due to lattice shrinkage caused by the incorporation of Rh atoms with a smaller atomic radius into the CeO_2 lattice.

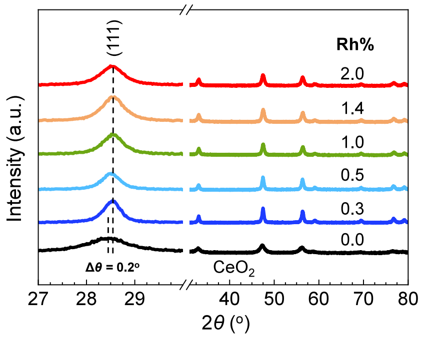

Figure 2. XRD patterns of Rh/CeO_2 catalysts (collected after CH_4 + O_2 treatment at 800 °C) with different loadings. The XRD pattern of CeO_2 calcined at 300 °C is shown for comparison.

The morphology of CeO_2 is observed by HRTEM images. CeO_2 has a rod-shaped morphology (Figure S3), and the fringe distance of the CeO_2 nanorods is 3.1 Å (Figure 3A), indicating that the CeO_2 nanorods mainly expose the (111) surface. Crystal lattices representing (−110) and (111) can be observed at the port of the nanorods (Figure 3B), indicating that the port growth direction is (11−2). In the STEM image of $0.3Rh/CeO_2$, a lattice spacing of 0.31 Å is also observed (Figure 3C), and no Rh nanoparticles are observed (Figure S4). On the thinner substrate, by detecting the intensity in the selected range, some spots with intensity changes (marked with yellow circles in Figure 3D) may possibly represent the existence of Rh single atoms. Meanwhile, the presence of Rh nanoparticles can be obviously observed in the STEM images of $2.0Rh/CeO_2$ (Figures 3E and S5), and the measured lattice distance of the Rh nanoparticles is 2.2 Å, which is characterized by the crystalline phase of Rh_2O_3 (Figure 3F). The average size of the counted Rh nanoparticles is about 1.8 nm (Figure S5). The support lattice spacing is 3.1 Å, indicating that Rh nanoparticles are loaded on the CeO_2 (111) surface.

We carried out CO adsorption DRIFT tests. As shown in Figure 4, CeO_2 does not generate obvious peaks ascribed to adsorbed CO. $0.3Rh/CeO_2$ shows obvious peaks at 2015 and 2083 cm^{-1}, ascribed to the asymmetric vibration peak and symmetric vibration peak of $Rh(CO)_2$, respectively.[30] These two peaks are always observed for single Rh atoms or small Rh clusters.[31] In addition to the above two peaks, $2.0Rh/CeO_2$ also shows a weak shoulder peak at 2060 cm^{-1} and a wide peak at 1800−1900 cm^{-1}, ascribed to the linear adsorption peak of Rh-CO[32] and the bridge adsorption peak of $Rh_2(CO)$,[31] respectively. The existence of the latter two peaks can be used as a direct evidence for the existence of Rh nanoparticles.[30]

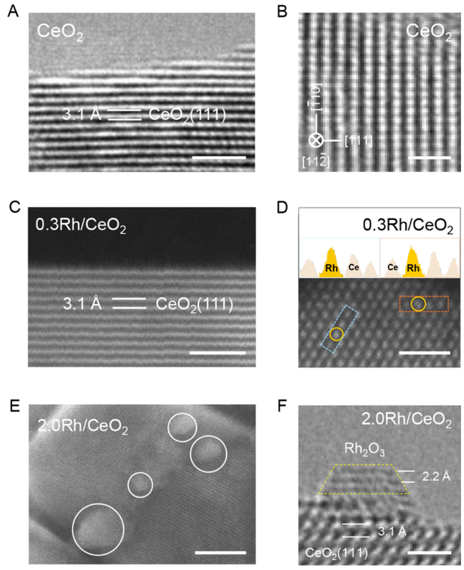

Figure 3. (A,B) HRTEM image of CeO_2. (C,D) STEM-ADF (annular dark field) images of $0.3Rh/CeO_2$ collected after CH_4 + O_2 treatment at 800 °C. (E) STEM-SE (secondary electron) and (F) STEM-ABF (annular bright field) images of $2.0Rh/CeO_2$ collected after CH_4 + O_2 treatment at 800 °C. The scale bar is 2 nm in parts A and C, 5 nm in part E, and 1 nm in parts B, D, and F.

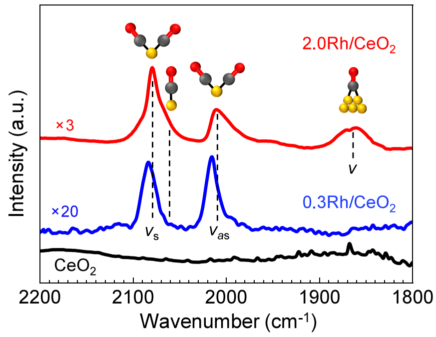

Figure 4. CO-DRIFT spectra of $2.0Rh/CeO_2$ and $0.3Rh/CeO_2$ collected after CH_4 + O_2 treatment at 800 °C. The spectrum of CeO_2 calcined at 300 °C is shown for comparison.

According to the bond angle formula of the infrared spectrum, the angle between two CO molecules can be calculated by using the area ratio of the asymmetric vibration peak (A_{asym}) and the symmetric vibration peak (A_{sym})[33] (Figure S6). When the Rh species exist as single atoms, the angle between the two CO molecules (2α) is close to 90°.[31,34] By integral statistics, the ratio of A_{asym}/A_{sym} on $0.3Rh/CeO_2$ is 0.98, and the corresponding 2α angle is 89°. The DRIFT data of $0.3Rh/CeO_2$ show the absence of the bridge adsorption peak of $Rh_2(CO)$, and the presence of two adsorption peaks of $Rh(CO)_2$, with an angle of ~90° between two CO molecules, indicates the presence of Rh single atoms on $0.3Rh/CeO_2$. In

https://doi.org/10.1021/acsomega.5c00062
ACS Omega 2025, 10, 18682−18689

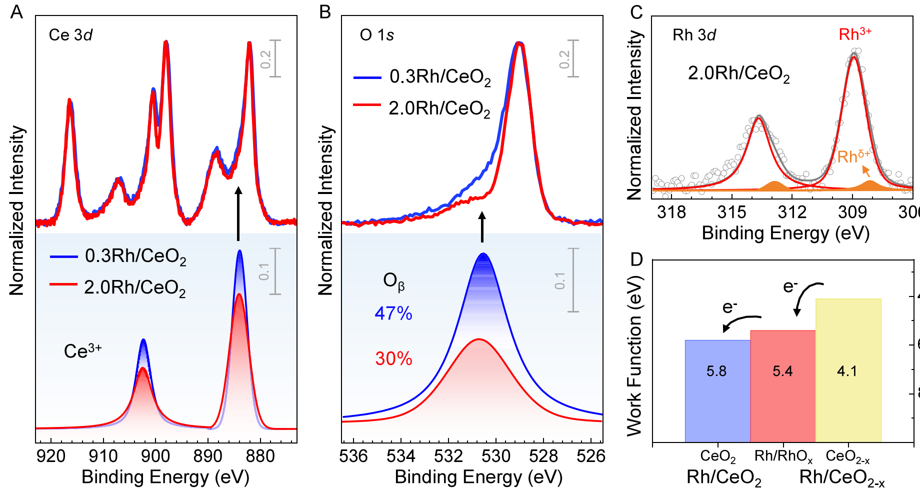

Figure 5. (A) Ce 3*d* and (B) O 1*s* XPS spectra of 0.3Rh/CeO_2 and 2.0Rh/CeO_2. (C) Rh 3*d* XPS spectra of 2.0Rh/CeO_2. (D) Electrons transferred from Rh to CeO_2 and from CeO_{2-x} to Rh. Ce 3d XPS and O 1s XPS fitting data are normalized with the strongest peak value of the origin spectrum. The binding energy of O 1s XPS of 2.0Rh/CeO_2 in (B) is shifted by 0.38 eV toward the lower energy, based on 0.3Rh/CeO_2. The upper spectra in (A) and (B) are the total spectra of each sample, and the bottom spectra are the fitting peaks representing Ce^{3+} and O_β, respectively. Rh/CeO_2 samples here refer to the catalysts collected after CH_4 + O_2 treatment at 800 °C.

the DRIFT data of 2.0Rh/CeO_2, the coexistence of bridge adsorption peaks and geminal adsorption peaks indicates that there are not only Rh nanoparticles but also Rh single atoms or small Rh clusters in 2.0Rh/CeO_2.

In order to study the cause of the change in catalytic activity, we investigated the electronic structures of 0.3Rh/CeO_2 and 2.0Rh/CeO_2 using XPS. The Ce 3*d* XPS data are shown in Figures 5A and S7. The proportions of the two groups of spin orbits can be calculated according to the peak fitting results.[35,36] The Ce^{3+} contents in 0.3Rh/CeO_2 and 2.0Rh/CeO_2 are 21 and 20%, respectively, showing a slight decrease in Ce^{3+} content. Similarly, from the peak fitting results of O 1*s* XPS (Figures 5B and S8), the proportions of chemisorbed oxygen (O_β)[37] in 0.3Rh/CeO_2 and 2.0Rh/CeO_2 are 47% and 30%, respectively, indicating that due to the existence of more Rh species in the form of Rh_2O_3, the lattice oxygen content in the catalyst is greatly increased, corresponding to the change of Ce^{3+} content.

The Rh 3*d* XPS spectra of 0.3Rh/CeO_2 and 2.0Rh/CeO_2 were obtained. The binding energy of Rh $3d_{5/2}$ in 0.3Rh/CeO_2 is around 309 eV, and no Rh^0 peak is observed (Figure S9), indicating that the Rh species is Rh^{3+} with a high oxidation state.[28,38] Two different Rh $3d_{5/2}$ peaks assignable to Rh^{3+} and $Rh^{\delta+}$ (~308 eV)[39] can be observed in the Rh 3*d* XPS spectra of 2.0Rh/CeO_2 (Figure 5C). The $Rh^{\delta+}$ species in 2.0Rh/CeO_2 is an intermediate valence between Rh^{3+} and Rh^0. Rh species in 2.0Rh/CeO_2 are predominantly Rh^{3+}, which does not seem to contradict the bridge adsorption peak observed in the CO−DRIFT spectra, as similar to ones reported in previous studies.[31,40]

In catalytic oxidation, CeO_2, as the oxygen storager, will undergo the transition between CeO_2 and CeO_{2-x}. The work function (ϕ) data of CeO_x at different stoichiometric ratios show that the extreme work functions of CeO_2 and CeO_{2-x} are about 5.8 and 4.1 eV, respectively.[41] The work functions of metallic Rh[42] and Rh_2O_3[43] are about 5.4 eV. As shown in Figure 5D, when the Ce and O contents in CeO_2 are close to the ideal stoichiometric ratio, electrons tend to transfer from Rh to CeO_2, electrons are stored in CeO_2, and reactive oxygen species are generated. While the work function of CeO_{2-x} formed after accepting electrons is significantly reduced, electrons can be transferred from CeO_{2-x} to Rh easily. Therefore, in the Rh/CeO_2 system, CeO_2 can not only store oxygen but also store electrons. The presence of partial $Rh^{\delta+}$ in 2.0Rh/CeO_2 endows the RhO_x nanoparticle with metallic properties,[44] which enables bidirectional electron transfer between Rh and CeO_2, that is, enhances electron transfer between metal active sites and the support. For the multielectron transfer process of CH_4 oxidation, the enhancement of electron transfer ability contributes to the acceleration of the reaction.

The influence of the electronic structure of the active site on catalytic activity was further studied by DFT calculations. First, theoretical models of nanoparticles and single-atom catalysts were constructed. Based on the HRTEM images of CeO_2 and STEM images of 0.3Rh/CeO_2 and 2.0Rh/CeO_2 in Figure 3, the CeO_2 support mainly exposes the {111} crystal surface, so we choose the CeO_2(111) surface as the substrate. According to the STEM images and Rh 3d XPS spectra of 2.0Rh/CeO_2, the Rh nanoparticles in 2.0Rh/CeO_2 exist in the form of Rh_2O_3 nanoparticles. In order to simplify the calculation, we first selected Rh_6O_9/CeO_2(111) for analysis. The theoretical size of Rh_6O_9 is about 1.0 nm, which is similar to the smallest nanoparticle size of 0.9 nm observed in the STEM images (Figure S5). We calculated the Bader charge of Rh atoms in Rh_6O_9/CeO_2(111), as shown in Figure S10. The six Rh atoms can be roughly divided into two types: one type is the high-valence Rh atom (Rh^{3+}), and the other type is the low-valence Rh atom ($Rh^{\delta+}$), which is consistent with the XPS results (Figure 5C). However, in our study, we cannot rule out the possibility that $Rh^{\delta+}$ is from another type of Rh single-atom species in 2.0Rh/CeO_2.

Since methane combustion occurs in an oxidizing atmosphere, we further considered different O-coordination situations, from Rh_6O_9 to Rh_6O_{12} structures, and calculated the Bader charge of Rh atoms. As shown in Figure S10, there are both some high-valence Rh atoms and some low-valence Rh atoms in each structure. We further calculated the phase diagram of each structure. As shown in Figure S11, Rh_6O_{12} shows better stability, so we chose Rh_6O_{12}/CeO_2(111) as the

https://doi.org/10.1021/acsomega.5c00062
ACS Omega 2025, 10, 18682−18689

reference model for the CeO_2-supported Rh nanoparticle catalyst (Figure S12).

For the single-atom catalyst model, taking into account the lattice shrinkage observed in Figure 2, we believe that Rh atoms are doped into the CeO_2(111) lattice. The XAS spectra of Rh foil and 0.3Rh/CeO_2 were measured, and we conducted extended X-ray absorption fine structure (EXAFS) analysis (Figures S13, S14 and Table S3). The shell with a distance of 2.03 Å and coordination numbers of ∼4.5 indicates that the isolated Rh atoms were anchored on the four-fold oxygen-terminated cavities. Therefore, we constructed the initial theoretical model as shown in Figure S15. Compared with the initial CeO_2(111) surface, the oxygen vacancy formation of the initial model decreased from 2.3 to 1.4 eV. At the same time, combined with the presence of a large percentage of O_β in Figure S8, the Rh_1/CeO_2(111)-O_V model containing an oxygen vacancy structure is finally selected as the model of the CeO_2-supported Rh single-atom catalyst (Figure S15), denoted as Rh_1/CeO_2, and its structure is consistent with the EXAFS results (Table S3).

We calculated the total density of state (DOS) of the Rh_6O_{12}/CeO_2 and Rh_1/CeO_2 surfaces, from which we can obtain the band gap ($\Delta\varepsilon$) between the lowest unoccupied band orbitals (LUBO) and the highest occupied band orbitals (HOBO) of the catalyst.[45] The results show that the total DOS of Rh_6O_{12}/CeO_2 and Rh_1/CeO_2 around the Fermi level (Figure 6A). For comparison, it can be observed that the LUBO and HOBO of Rh_6O_{12}/CeO_2 are almost connected near the Fermi level, with a gap of about 0 eV, while the gap of Rh_1/CeO_2 is about 0.6 eV. According to front-band orbital theory,[46] a smaller $\Delta\varepsilon$ value is more conducive to electron transfer in the reaction process and the activation of reactants, resulting in higher catalytic activity. It can be seen from the change of the gap between the LUBO and the HOBO that the single-atom catalyst shows nonmetallic properties, while the nanoparticle catalyst shows metallic properties. This difference leads to a change of electron transfer ability of the catalyst, resulting in higher catalytic activity for CH_4 oxidation over Rh nanoparticle catalysts.

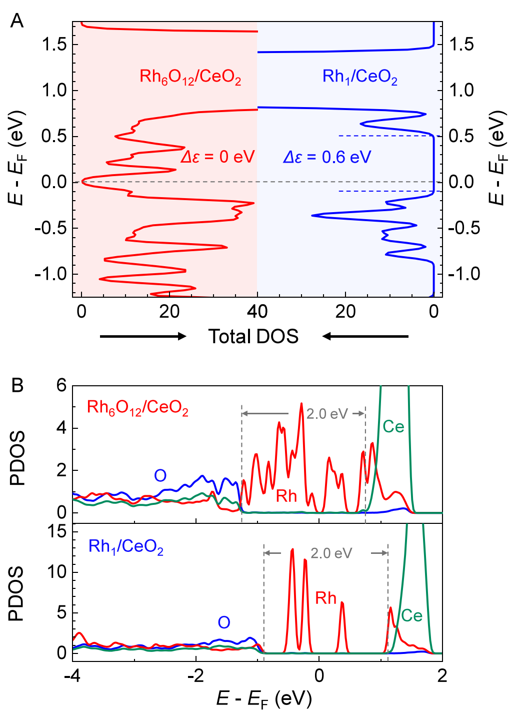

Figure 6. (A) Calculated total density of states (DOS) of Rh_6O_{12}/CeO_2 and Rh_1/CeO_2 around the Fermi level together with the $\Delta\varepsilon$ values. (B) Calculated partial DOS (PDOS) of the O, Rh, and Ce of Rh_6O_{12}/CeO_2.

In order to study the contribution of the Rh/CeO_2 system to the DOS of the LUBO and HOBO, the partial DOS of Rh, Ce, and O for Rh_6O_{12}/CeO_2 and Rh_1/CeO_2 were calculated. As shown in Figure 6B, a large gap of ∼2.0 eV can be found between the highest occupied state and the lowest unoccupied state of the CeO_2 support, and the Rh DOS essentially fills the whole bandgap and contributes to the HOBO−LUBO region. The results line well with the reported literature.[47] The unoccupied states of the CeO_2 support are mainly located at ∼0.8 eV above the Fermi level, which can serve as electron acceptors. In the region above the Fermi level, a high overlap of the unoccupied states of Rh, O, and Ce can be observed. As the LUBO of Rh nanoparticles accepts electrons from CH_4, these electrons can be transferred to the LUBO of CeO_2 for storage, thus accelerating CH_4 oxidation and producing Ce^{3+}. When the electrons of Rh are transferred to O_2 for activation, the high-energy-level $4f^1$ electrons can also be easily transferred to Rh nanoparticles, thus accelerating O_2 activation. However, in Rh_1/CeO_2, a large gap of ∼2.0 eV still exists between the highest occupied state and the lowest unoccupied state of the CeO_2 support. The partial DOS of a Rh single atom does not fully fill the gap, and there is a certain energy barrier required in the bidirectional electron transfer process. Therefore, the metallic properties of the Rh nanoparticle catalyst are mainly contributed by the electron states of Rh nanoparticles near the Fermi level. The synergistic effect of high-density Rh-occupied states and the unoccupied states of Ce together promotes the activity of catalytic CH_4 oxidation, which cannot be provided by single-atom active sites.

On the basis of the above, we calculated the first C−H bond dissociation in CH_4 on Rh_6O_{12}/CeO_2 and Rh_1/CeO_2, that is, the rate-determining step[5,48] (Figure 7). First, the adsorption of CH_4 on the two surfaces is considered. The calculated results show that the adsorption of CH_4 is weak for the two models, with reaction exotherms of 0.01 and 0.02 eV, respectively. Then, the dissociation of CH_4 at Rh_6O_{12} and Rh_1 sites is considered to form Rh-CH_3 and the O−H species. The calculated energy barrier of the first C−H bond of CH_4 dissociation on Rh_1/CeO_2 is 0.93 eV, while that on Rh_6O_{12}/CeO_2 is 0.77 eV, significantly easier to active CH_4. Finally, after the C−H bond breaks and steady state forms, the enthalpy changes of this step on Rh_6O_{12}/CeO_2 and Rh_1/CeO_2 are −1.21 and −0.78 eV, respectively. Based on Van't Hoff equation, the greater the enthalpy changes of an exothermic reaction process, the greater the equilibrium constant of the reaction, that is, the more the reaction trends to proceed in the direction of the forward reaction. The differences of activation energy barrier (−0.16 eV) and activation enthalpy change (−0.43 eV) both indicate that Rh_6O_{12}/CeO_2 has a stronger activation capacity of CH_4 and better ability of stable dissociation products than Rh_1/CeO_2, which is conducive to the subsequent reaction.

The objective of this research is to study the effect of Rh loading on the performance of Rh/CeO_2 catalysts. Although the activity of 2.0Rh/CeO_2 in this research is not as high as some other nanoparticle catalysts reported[9,12] (Table S4), our results show that, in CH_4 oxidation, the activity of CeO_2-basd

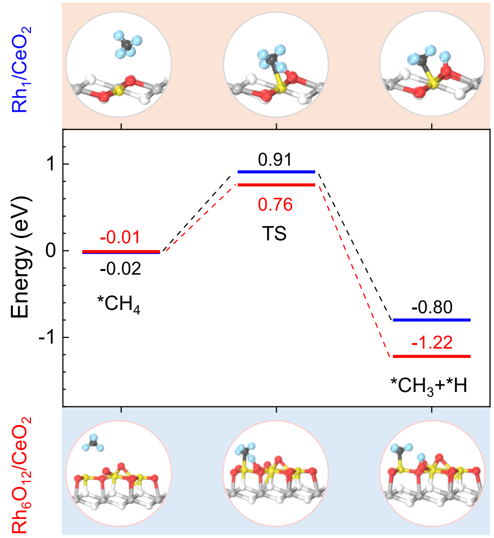

Figure 7. Calculated energy profiles of the first C−H bond dissociation in CH_4 on Rh_6O_{12}/CeO_2 (red) and Rh_1/CeO_2 (blue). Inset: the calculated structure (side view) of the initial, transition, and final states of the first C−H bond cleavage of CH_4 on Rh_1/CeO_2 and Rh_6O_{12}/CeO_2.

Rh nanoparticles is higher than that of Rh single atoms. The same trend was also reported in studies of Pd[49,50] and Pt catalysts[45] in CH_4 oxidation. It should be mentioned that this trend does not apply to all reactions or all catalyst systems, especially in reactions that require high selectivity. In the selective oxidation of formic acid, a two-electron process occurs on a titanium nitride-supported Pt single-atom catalyst, which shows higher H_2O_2 mass activity than the traditional four-electron process of the Pt nanoparticle catalyst.[51] In CO_2 hydrogenation, the methanol selectivity of the Pt single-atom catalyst is higher than that of the Pt nanoparticle catalyst based on different reaction paths.[52] For the oxidation reactions, the reaction rate of the multielectron process has higher requirements for the electron transfer rate. For example, in the catalytic oxidation of benzene, the activity of Pt nanoparticles supported on CeO_2 is significantly higher than that of the Pt single-atom catalyst.[45] In CO oxidation, Rh nanoparticles,[44] Pt nanoparticles,[53] and Ag nanoparticles[54] supported on Al_2O_3 also show higher activity than the corresponding single-atom catalysts. Similarly, the main conclusion in our work is that the difference in the electronic state accompanied by the different active sites leads to the difference in activity.

4. CONCLUSIONS

In this study, we compared the catalytic activities in CH_4 oxidation of Rh/CeO_2 with different Rh loadings. With the increase of Rh loading (from 0.3 to 2.0 wt %), the catalytic activities increase. $0.3Rh/CeO_2$ and $2.0Rh/CeO_2$ were selected as representative samples. Combining STEM images and DRIFT data, it could be deduced that $0.3Rh/CeO_2$ has Rh single atoms, and $2.0Rh/CeO_2$ has both Rh single atoms and RhO_x nanoparticles. By combining the characteristic data and theoretical calculations, we can conclude that the coexistence of Rh^{3+} and $Rh^{\delta+}$ in RhO_x nanoparticles and smaller band gaps in frontier band orbitals render the CeO_2-supported RhO_x nanoparticle catalyst more favorable for the electron transfer, resulting in a lower energy barrier in the C−H bond activation process and higher methane oxidation activity than the Rh single-atom catalyst.

■ ASSOCIATED CONTENT

Supporting Information

The Supporting Information is available free of charge at https://pubs.acs.org/doi/10.1021/acsomega.5c00062.

Calculation of the theoretical maximum Rh single atom loading, repeatability tests, TEM images, STEM-SE and STEM-ADF images, XPS spectra, calculated structures and Bader charge, XANES spectra, ICP results, EXAFS fitting parameters, and comparison of catalysts activity (PDF)

■ AUTHOR INFORMATION

Corresponding Authors

Yaxin Chen − *Department of Environmental Science and Engineering, Fudan University, Shanghai 200438, China;* Email: chenyaxin@fudan.edu.cn

Xingfu Tang − *Department of Environmental Science and Engineering, Fudan University, Shanghai 200438, China; Jiangsu Collaborative Innovation Center of Atmospheric Environment and Equipment Technology, Nanjing University of Information Science and Technology, Nanjing 210044, China; Shanghai Institute of Pollution Control and Ecological Security, Shanghai 200092, China;* orcid.org/0000-0002-0746-1294; Email: tangxf@fudan.edu.cn

Xi Liu − *School of Chemistry and Chemical Engineering, Ningxia University, Yinchuan 750021, China; School of Chemistry and Chemical Engineering, In Situ Center for Physical Sciences, Frontiers Science Center for Transformative Molecules, Shanghai Jiao Tong University, Shanghai 200240, China;* orcid.org/0000-0002-8654-0774; Email: liuxi@sjtu.edu.cn

Xue-Qing Gong − *School of Chemistry and Chemical Engineering, Shanghai Jiao Tong University, Shanghai 200240, China;* orcid.org/0000-0002-9566-7427; Email: xqgong@sjtu.edu.cn

Zhen Ma − *Department of Environmental Science and Engineering, Fudan University, Shanghai 200438, China; Shanghai Institute of Pollution Control and Ecological Security, Shanghai 200092, China;* orcid.org/0000-0002-2391-4943; Email: zhenma@fudan.edu.cn

Authors

Chenxin Xu − *Department of Environmental Science and Engineering, Fudan University, Shanghai 200438, China*

Tian Qin − *School of Chemistry and Chemical Engineering, In Situ Center for Physical Sciences, Frontiers Science Center for Transformative Molecules, Shanghai Jiao Tong University, Shanghai 200240, China;* orcid.org/0000-0002-2856-4743

Ze-Kai Yu − *State Key Laboratory of Green Chemical Engineering and Industrial Catalysis, Centre for Computational Chemistry and Research Institute of Industrial Catalysis, School of Chemistry and Molecular Engineering, East China University of Science and Technology, Shanghai 200237, China*

Zhi-Qiang Wang − *State Key Laboratory of Green Chemical Engineering and Industrial Catalysis, Centre for Computational Chemistry and Research Institute of Industrial Catalysis, School of Chemistry and Molecular*

Engineering, East China University of Science and Technology, Shanghai 200237, China; orcid.org/0000-0001-6293-1474

Liwei Chen − *School of Chemistry and Chemical Engineering, In Situ Center for Physical Sciences, Frontiers Science Center for Transformative Molecules, Shanghai Jiao Tong University, Shanghai 200240, China;* orcid.org/0000-0003-4160-9771

Complete contact information is available at: https://pubs.acs.org/10.1021/acsomega.5c00062

Author Contributions

○C.X., T.Q., Z.-K.Y., and Z.-Q.W. contributed equally.

Notes

The authors declare no competing financial interest.

■ ACKNOWLEDGMENTS

This work is supported by the National Key R&D Program of China (2022YFB3504100, 2023YFA1508500, 2021YFA1500700, 2021YFA1500300, and 2022YFA1500146), the National Natural Science Foundation of China (22276036, 22276037, 22203030, 22272106, and 22072090), and the Shanghai Sailing Program (24YF2702100).

■ REFERENCES

(1) He, L.; Fan, Y.; Bellettre, J.; Yue, J.; Luo, L. A review on catalytic methane combustion at low temperatures: Catalysts, mechanisms, reaction conditions and reactor designs. *Renew. Sust. Energy Rev.* **2020**, *119*, No. 109589.

(2) Jiang, D.; Khivantsev, K.; Wang, Y. Low-temperature methane oxidation for efficient emission control in natural gas vehicles: Pd and beyond. *ACS Catal.* **2020**, *10* (23), 14304−14314.

(3) Tang, Z.; Zhang, T.; Luo, D.; Wang, Y.; Hu, Z.; Yang, R. T. Catalytic combustion of methane: from mechanism and materials properties to catalytic performance. *ACS Catal.* **2022**, *12* (21), 13457−13474.

(4) Feng, X.; Jiang, L.; Li, D.; Tian, S.; Zhu, X.; Wang, H.; He, C.; Li, K. Progress and key challenges in catalytic combustion of lean methane. *J. Energy Chem.* **2022**, *75*, 173−215.

(5) Trinchero, A.; Hellman, A.; Grönbeck, H. Methane oxidation over Pd and Pt studied by DFT and kinetic modeling. *Surf. Sci.* **2013**, *616*, 206−213.

(6) Wang, Y.; Hu, P.; Yang, J.; Zhu, Y.-A.; Chen, D. C-H bond activation in light alkanes: a theoretical perspective. *Chem. Soc. Rev.* **2021**, *50* (7), 4299−4358.

(7) Au, C.-T.; Ng, C.-F.; Liao, M.-S. Methane dissociation and syngas formation on Ru, Os, Rh, Ir, Pd, Pt, Cu, Ag, and Au: a theoretical study. *J. Catal.* **1999**, *185* (1), 12−22.

(8) Oh, S. H.; Mitchell, P. J.; Siewert, R. M. Methane oxidation over alumina-supported noble metal catalysts with and without cerium additives. *J. Catal.* **1991**, *132* (2), 287−301.

(9) Burch, R.; Loader, P. K. An investigation of the use of zirconia as a support for rhodium catalysts. *Appl. Catal. A-Gen.* **1996**, *143* (2), 317−335.

(10) Hurtado, P.; Ordóñez, S.; Vega, A.; Diez, F. V. Catalytic combustion of methane over commercial catalysts in presence of ammonia and hydrogen sulphide. *Chemosphere* **2004**, *55* (5), 681−689.

(11) Kumsung, W.; Chareonpanich, M.; Kongkachuichay, P.; Senkan, S.; Seubsai, A. Single and bimetallic catalyst screenings of noble metals for methane combustion. *Catal. Commun.* **2018**, *110*, 83−87.

(12) Zhang, Y.; Glarborg, P.; Andersson, M. P.; Johansen, K.; Torp, T. K.; Jensen, A. D.; Christensen, J. M. Influence of the support on rhodium speciation and catalytic activity of rhodium-based catalysts for total oxidation of methane. *Catal. Sci. Technol.* **2020**, *10* (17), 6035−6044.

(13) Zhang, Y.; Glarborg, P.; Andersson, M. P.; Johansen, K.; Torp, T. K.; Jensen, A. D.; Christensen, J. M. Sulfur poisoning and regeneration of Rh-ZSM-5 catalysts for total oxidation of methane. *Appl. Catal., B* **2020**, *277*, No. 119176.

(14) Akbari, E.; Alavi, S. M.; Rezaei, M.; Larimi, A. Preparation and evaluation of A/BaO-MnO catalysts (A: Rh, Pt, Pd, Ru) in lean methane catalytic combustion at low temperature. *Int. J. Energy Res.* **2022**, *46* (5), 6292−6313.

(15) Liu, Y.; Peng, Y.; Naschitzki, M.; Gewinner, S.; Schöllkopf, W.; Kuhlenbeck, H.; Pentcheva, R.; Roldan Cuenya, B. Surface oxygen vacancies on reduced Co_3O_4(100): superoxide formation and ultra-low-temperature CO oxidation. *Angew. Chem., Int. Ed.* **2021**, *60* (30), 16514−16520.

(16) Esch, F.; Fabris, S.; Zhou, L.; Montini, T.; Africh, C.; Fornasiero, P.; Comelli, G.; Rosei, R. Electron localization determines defect formation on ceria substrates. *Science* **2005**, *309* (5735), 752−755.

(17) Campbell, C. T.; Peden, C. H. F. Oxygen vacancies and catalysis on ceria surfaces. *Science* **2005**, *309* (5735), 713−714.

(18) Muravev, V.; Parastaev, A.; van den Bosch, Y.; Ligt, B.; Claes, N.; Bals, S.; Kosinov, N.; Hensen, E. J. M. Size of cerium dioxide support nanocrystals dictates reactivity of highly dispersed palladium catalysts. *Science* **2023**, *380* (6650), 1174−1179.

(19) Mai, H.-X.; Sun, L.-D.; Zhang, Y.-W.; Si, R.; Feng, W.; Zhang, H.-P.; Liu, H.-C.; Yan, C.-H. Shape-selective synthesis and oxygen storage behavior of ceria nanopolyhedra, nanorods, and nanocubes. *J. Phys. Chem. B* **2005**, *109* (51), 24380−24385.

(20) Perdew, J. P.; Burke, K.; Ernzerhof, M. Generalized gradient approximation made simple. *Phys. Rev. Lett.* **1996**, *77* (18), 3865−3868.

(21) Teter, M. P.; Payne, M. C.; Allan, D. C. Solution of Schrödinger's equation for large systems. *Phys. Rev. B* **1989**, *40* (18), 12255−12263.

(22) Kümmerle, E. A.; Heger, G. The structures of C-$Ce_2O_{3+\delta}$, Ce_7O_{12}, and $Ce_{11}O_{20}$. *J. Soild State Chem.* **1999**, *147* (2), 485−500.

(23) Jerratsch, J.-F.; Shao, X.; Nilius, N.; Freund, H.-J.; Popa, C.; Ganduglia-Pirovano, M. V.; Burow, A. M.; Sauer, J. Electron localization in defective ceria films: A study with scanning-tunneling microscopy and density-functional theory. *Phys. Rev. Lett.* **2011**, *106* (24), No. 246801.

(24) Nolan, M.; Grigoleit, S.; Sayle, D. C.; Parker, S. C.; Watson, G. W. Density functional theory studies of the structure and electronic structure of pure and defective low index surfaces of ceria. *Surf. Sci.* **2005**, *576* (1), 217−229.

(25) Nolan, M.; Parker, S. C.; Watson, G. W. The electronic structure of oxygen vacancy defects at the low index surfaces of ceria. *Surf. Sci.* **2005**, *595* (1), 223−232.

(26) Jones, J.; Xiong, H.; DeLaRiva, A. T.; Peterson, E. J.; Pham, H.; Challa, S. R.; Qi, G.; Oh, S.; Wiebenga, M. H.; Pereira Hernández, X. I.; Wang, Y.; Datye, A. K. Thermally stable single-atom platinum-on-ceria catalysts via atom trapping. *Science* **2016**, *353* (6295), 150−154.

(27) Jiang, D.; Wan, G.; Halldin Stenlid, J.; García-Vargas, C. E.; Zhang, J.; Sun, C.; Li, J.; Abild-Pedersen, F.; Tassone, C. J.; Wang, Y. Dynamic and reversible transformations of subnanometre-sized palladium on ceria for efficient methane removal. *Nat. Catal.* **2023**, *6* (7), 618−627.

(28) Bai, S.; Liu, F.; Huang, B.; Li, F.; Lin, H.; Wu, T.; Sun, M.; Wu, J.; Shao, Q.; Xu, Y.; Huang, X. High-efficiency direct methane conversion to oxygenates on a cerium dioxide nanowires supported rhodium single-atom catalyst. *Nat. Commun.* **2020**, *11* (1), No. 954.

(29) Aitbekova, A.; Wrasman, C. J.; Riscoe, A. R.; Kunz, L. Y.; Cargnello, M. Determining number of sites on ceria stabilizing single atoms via metal nanoparticle redispersion. *Chin. J. Catal.* **2020**, *41* (6), 998−1005.

(30) Shan, J.; Li, M.; Allard, L. F.; Lee, S.; Flytzani-Stephanopoulos, M. Mild oxidation of methane to methanol or acetic acid on

supported isolated rhodium catalysts. *Nature* **2017**, *551* (7682), 605−608.

(31) Kwon, Y.; Kim, T. Y.; Kwon, G.; Yi, J.; Lee, H. Selective activation of methane on single-atom catalyst of rhodium dispersed on zirconia for direct conversion. *J. Am. Chem. Soc.* **2017**, *139* (48), 17694−17699.

(32) Yang, L.; Li, X.; He, H.; Liu, T.; Wang, W.; Yang, Z.; Li, S.; Li, J.; Liu, B. Enhanced low-temperature activity of Rh-Pt alloy clusters supported on TiO_2/Ti nanosheets for selective catalytic reduction of NO by CO. *Appl. Surf. Sci.* **2025**, *695*, No. 162824.

(33) Kettle, S. F. A.; Paul, I., Infrared intensities of metal carbonyl stretching vibrations. In *Adv. Organomet. Chem.*; Stone, F. G. A.; West, R., Eds.; Academic Press: 1972; Vol. *10*, pp 199−236.

(34) Yang, C.; Garl, C. W. Infrared studies of carbon monoxide chemisorbed on rhodium. *J. Phys. Chem.* **1957**, *61* (11), 1504−1512.

(35) Gao, X.; Jiang, Y.; Zhong, Y.; Luo, Z.; Cen, K. The activity and characterization of CeO_2-TiO_2 catalysts prepared by the sol-gel method for selective catalytic reduction of NO with NH_3. *J. Hazadr. Mater.* **2010**, *174* (1), 734−739.

(36) Liu, C.; Chen, L.; Li, J.; Ma, L.; Arandiyan, H.; Du, Y.; Xu, J.; Hao, J. Enhancement of activity and sulfur resistance of CeO_2 supported on TiO_2-SiO_2 for the selective catalytic reduction of NO by NH_3. *Environ. Sci. Technol.* **2012**, *46* (11), 6182−6189.

(37) Yun, L.-X.; Wu, H.; Shen, Z.-G.; Fu, J.-W.; Wang, J.-X. Ultrasmall CeO_2 nanoparticles with rich oxygen defects as novel catalysts for efficient glycolysis of polyethylene terephthalate. *ACS Sustain. Chem. Eng.* **2022**, *10* (16), 5278−5287.

(38) Wang, L.; Zhang, W.; Wang, S.; Gao, Z.; Luo, Z.; Wang, X.; Zeng, R.; Li, A.; Li, H.; Wang, M.; Zheng, X.; Zhu, J.; Zhang, W.; Ma, C.; Si, R.; Zeng, J. Atomic-level insights in optimizing reaction paths for hydroformylation reaction over Rh/CoO single-atom catalyst. *Nat. Commun.* **2016**, *7* (1), No. 14036.

(39) Machida, M.; Minami, S.; Hinokuma, S.; Yoshida, H.; Nagao, Y.; Sato, T.; Nakahara, Y. Unusual redox behavior of Rh/$AlPO_4$ and its impact on three-way catalysis. *J. Phys. Chem. C* **2015**, *119* (1), 373−380.

(40) Wu, D.; Liu, S.; Zhong, M.; Zhao, J.; Du, C.; Yang, Y.; Sun, Y.; Lin, J.; Wan, S.; Wang, S.; Huang, J.; Yao, Y.; Li, Z.; Xiong, H. Nature and dynamic evolution of Rh single atoms trapped by CeO_2 in CO hydrogenation. *ACS Catal.* **2022**, *12* (19), 12253−12267.

(41) Wardenga, H. F.; Klein, A. Surface potentials of (111), (110) and (100) oriented CeO_{2-x} thin films. *Appl. Surf. Sci.* **2016**, *377*, 1−8.

(42) Fu, Q.; Wagner, T.; Olliges, S.; Carstanjen, H.-D. Metal-oxide interfacial reactions: encapsulation of Pd on TiO_2 (110). *J. Phys. Chem. B* **2005**, *109* (2), 944−951.

(43) Kumar Manna, B.; Samanta, R.; Kumar Trivedi, R.; Chakraborty, B.; Barman, S. Hydrogen spillover inspired bifunctional platinum/rhodium oxide-nitrogen-doped carbon composite for enhanced hydrogen evolution and oxidation reactions in base. *J. Colloid Interface Sci.* **2024**, *670*, 258−271.

(44) Xu, D.; Jin, Y.; He, B.; Fang, X.; Chen, G.; Qu, W.; Xu, C.; Chen, J.; Ma, Z.; Chen, L.; Tang, X.; Liu, X.; Wei, G.; Chen, Y. Electronic communications between active sites on individual metallic nanoparticles in catalysis. *Nat. Commun.* **2024**, *15* (1), No. 8614.

(45) Liu, J.; Fang, X.; Liu, D.; Hu, X.; Qin, T.; Chen, J.; Liu, R.; Xu, D.; Qu, W.; Dong, Y.; Chen, L.; Ma, Z.; Liu, X.; Li, X.; Tang, X. Benzene abatement catalyzed by ceria-supported platinum nanoparticles and single atoms. *Chem. Eng. J.* **2023**, *467*, No. 143407.

(46) Xu, D.; Qu, W.; Gu, X.; Li, M.; Liu, R.; Dong, Y.; Ma, Z.; Chen, Y.; Tang, X. An activity descriptor for perovskite oxides in catalysis. *Chem. Catal.* **2022**, *2* (5), 1163−1176.

(47) Vayssilov, G. N.; Lykhach, Y.; Migani, A.; Staudt, T.; Petrova, G. P.; Tsud, N.; Skála, T.; Bruix, A.; Illas, F.; Prince, K. C.; Matolın, V. R.; Neyman, K. M.; Libuda, J. Support nanostructure boosts oxygen transfer to catalytically active platinum nanoparticles. *Nat. Mater.* **2011**, *10* (4), 310−315.

(48) Hu, W.; Lan, J.; Guo, Y.; Cao, X.-M.; Hu, P. Origin of efficient catalytic combustion of methane over Co_3O_4(110): active low-coordination lattice oxygen and cooperation of multiple active sites. *ACS Catal.* **2016**, *6* (8), 5508−5519.

(49) Chen, S.; Li, S.; You, R.; Guo, Z.; Wang, F.; Li, G.; Yuan, W.; Zhu, B.; Gao, Y.; Zhang, Z.; Yang, H.; Wang, Y. Elucidation of active sites for CH_4 catalytic oxidation over Pd/CeO_2 via tailoring metal-support interactions. *ACS Catal.* **2021**, *11* (9), 5666−5677.

(50) Xiong, H.; Kunwar, D.; Jiang, D.; García-Vargas, C. E.; Li, H.; Du, C.; Canning, G.; Pereira-Hernandez, X. I.; Wan, Q.; Lin, S.; Purdy, S. C.; Miller, J. T.; Leung, K.; Chou, S. S.; Brongersma, H. H.; ter Veen, R.; Huang, J.; Guo, H.; Wang, Y.; Datye, A. K. Engineering catalyst supports to stabilize PdO_x two-dimensional rafts for water-tolerant methane oxidation. *Nat. Catal.* **2021**, *4* (10), 830−839.

(51) Yang, S.; Kim, J.; Tak, Y. J.; Soon, A.; Lee, H. Single-atom catalyst of platinum supported on titanium nitride for selective electrochemical reactions. *Angew. Chem., Int. Ed.* **2016**, *55* (6), 2058−2062.

(52) Chen, Y.; Li, H.; Zhao, W.; Zhang, W.; Li, J.; Li, W.; Zheng, X.; Yan, W.; Zhang, W.; Zhu, J.; Si, R.; Zeng, J. Optimizing reaction paths for methanol synthesis from CO_2 hydrogenation via metal-ligand cooperativity. *Nat. Commun.* **2019**, *10* (1), No. 1885.

(53) Ding, K.; Gulec, A.; Johnson, A. M.; Schweitzer, N. M.; Stucky, G. D.; Marks, L. D.; Stair, P. C. Identification of active sites in CO oxidation and water-gas shift over supported Pt catalysts. *Science* **2015**, *350* (6257), 189−192.

(54) Wang, F.; Li, Z.; Wang, H.; Chen, M.; Zhang, C.; Ning, P.; He, H. Nano-sized Ag rather than single-atom Ag determines CO oxidation activity and stability. *Nano Res.* **2022**, *15* (1), 452−456.